Chemical Engineering Journal 414 (2021) 128638

Contents lists available at ScienceDirect

Chemical Engineering Journal

journal homepage: www.elsevier.com/locate/cej

High-mass-loading Sn-based anode boosted by pseudocapacitance for long-life sodium-ion batteries

Wei He [a], Ke Chen [a], Rajesh Pathak [a], Matthew Hummel [b], Khan Mamun Reza [a], Nabin Ghimire [a], Jyotshna Pokharel [a], Shun Lu [b], Zhengrong Gu [b], Qiquan Qiao [c], Yue Zhou [a,*]

[a] Department of Electrical Engineering and Computer Science, South Dakota State University, Brookings, SD 57007, USA
[b] Department of Agricultural and Biosystems Engineering, South Dakota State University, Brookings, SD 57007, USA
[c] Department of Mechanical and Aerospace Engineering, Syracuse University, NY 13244, USA

ARTICLE INFO

Keywords:
Free-standing anode
High mass loading
Pseudocapacitive contribution
Sodium ion batteries

ABSTRACT

Sodium-ion batteries (SIBs) are considered as a promising alternative to lithium-ion batteries in large-scale energy storage due to the abundant sodium resources and low cost. However, the practical applications are still hindered by several factors such as limited cycling life and low mass loading of the electrode. Herein, a uniform free-standing Sn-based (Sn@CFC) electrode was synthesized *via* a facile electrospinning method. The cross-link nitrogen-doped carbon fiber and ultrasmall metallic Sn nanoparticles together provide fast ions and electrons pathway, enabling a dominant pseudocapacitance contribution of 87.1% at a scan rate of 0.5 mV s^{-1}. The Sn@CFC electrode hence exhibits a high reversible area capacity of 1.68 mAh cm^{-2} at 50 mA g^{-1} and long cycle life of 1000 cycles at 200 mA g^{-1} with more than 80% capacity retention. Moreover, the facile manufacturing technique yields the Sn@CFC electrode with an extremely high mass loading of 5.5 mg cm^{-2} with very little sacrifice of electrochemical performances. This study provides a promising route to scalably fabricate electrodes with high area capacity and high energy density for advanced SIBs.

1. Introduction

To meet the ever-growing demands for portable electronics, electric vehicles (EVs) and large-scale energy storage, many secondary battery systems have been developed. State-of-the-art (SOA) lithium-ion batteries (LIBs) attract the most attention and dominate the market due to their high energy density and long cycle life [1,2]. However, the fact that the scarcity and uneven geographical distribution of lithium resources makes LIBs quite expensive and limits their application in large-scale energy storage [3,4]. Alternatively, sodium-ion batteries (SIBs) are considered to replace LIBs in large-scale stationary energy storage systems, since the sodium is earth-abundant and cost-effective element [5–7]. It is noted that graphite anode materials, which are widely used in LIBs with a theoretical specific capacity of 372 mAh g^{-1}, low charge/discharge plateau potential, and good cycling ability, fail in SIBs system [8–10]. This is because the radius of Na ions is larger than that of Li ions (0.102 nm vs 0.076 nm), which directly affects the mass transport and storage in the electrochemical process [11–14]. Hence, it is urgent to develop an abundant, stable, and highly conductive anode for SIBs to catch up the energy density of LIBs [15].

Among the anodes, metallic tin (Sn) is considered as a promising anode due to its high theoretical capacity of 847 mAh g^{-1}, as well as its low cost and environmental friendliness [16,17]. However, the metallic Sn electrode suffers a 420% expansion during the sodiation/desodiation processes, resulting in continuous pulverization of active materials and then the loss of electrical contact with the current collector [18–20]. That will lead to a fast capacity fading and prevent its practical application in SIBs. To address those issues, many strategies have been developed, such as designing a core-shell structure [21,22], fabricating Sn-based alloy [23,24], and forming Sn/C composite [25–27]. Moreover, downsizing the Sn particles to the nanoscale has been demonstrated to be an effective way to alleviate strain during the large volume changes and improve the cycling stability. The nano-size Sn materials can be further modified by coating with carbon materials, which act as a buffer layer to mitigate fracture during volume changes, enhance mechanical integrity, and improve electrical conductivity. For example, Chen's group reported a Sn/C composite by aerosol spray pyrolysis, where the nano-sized Sn particles were finely embedded in spherical

* Corresponding author.
E-mail address: yue.zhou@sdstate.edu (Y. Zhou).

https://doi.org/10.1016/j.cej.2021.128638
Received 5 November 2020; Received in revised form 22 December 2020; Accepted 18 January 2021
Available online 23 January 2021
1385-8947/Published by Elsevier B.V.

carbon network, delivering a stable capacity during prolonged cycling up to 500 cycles [28]. Despite those successes, there are still some issues remaining, influencing further industrial applications. First, there is still a big challenge to employ conventional methods to fabricate nano-size Sn/C with high mass loading although it is significant for high gravimetric or volumetric energy density based on the whole cell. It is noted that the reported mass loading of common anode of SIBs in the SOA literature is smaller than 2 mg cm^{-2} [26,29–31]. Second, Sn/C electrode fabricated by traditional roll-to-roll coating process easily delaminated from the current collector due to their weak adhesion [32,33]. Moreover, it is difficult for the electrolyte to diffuse into the electrode with a high mass, resulting in the considerable increase of the cell impedance and the loss of energy efficiency [33,34]. Therefore, it is desired to develop scalable manufacturing techniques to synthesize nano-size Sn/C without current collector by reducing manufacturing steps and costs, enabling applications for large scale energy storage systems.

Herein, we report an advanced anode with nano-sized metallic Sn nanoparticles finely decorated on the carbon fiber cloth (Sn@CFC) by a scalable electrospinning method. This unique process produces Sn@CFC electrode with extremely high mass loading of 5.5 mg cm^{-2} and homogeneous nanomorphology. The ultrasmall Sn particles can shorten the diffusion pathway of ions and electrons and can alleviated strain during sodiation/desodiation. Moreover, the carbon fibers with nitrogen doping not only provide the electrons and ions transfer path to dramatically enhance the conductivity, but also act as the buffer layer to keep the structure of metallic Sn particles stable during the volume variation. It is found that the Sn nanoparticles and carbon fiber together give rise to a dominant pseudocapacitance contribution of 87.1% at a scan rate of 0.5 mV s^{-1}, which can overcome slow diffusion-limited redox mechanism in active materials to lead to good electrochemical performance. As a result, the free-standing Sn@CFC anode shows a high reversible areal capacity of 1.68 mAh cm^{-2} which is much larger or competitive compared with reported SOA nano-sized anode materials [13,14,35,36]. Meanwhile, it exhibits a long cycle life of 1000 cycles with more than 80% capacity retention.

2. Experimental section

2.1. Preparation of free-standing Sn@CFC

Firstly, 474 mg tin (II) chloride ($SnCl_2$, Sigma Aldrich) was dissolved into 5 mL N, N-dimethylformamide (DMF). Then, 265 mg sodium carbonate (Na_2CO_3, Sigma Aldrich) was added slowly to the solution followed by stirring 1 h. After that, 300 mg polyacrylonitrile (PAN, Sigma Aldrich) was dispersed into the obtained light-yellow solution to form a homogeneous SnO/PAN mixture under vigorous stirring for 10 h. The mixture was stood still for another 1 h and the as-obtained supernatant was used as the precursor for electrospinning. The precursor solution was loaded into a 3 mL syringe pump with a flattop stainless-steel needle and spun at a rate of 0.5 mL h^{-1}. A voltage of 10 kV and a distance of 10 cm between the needle and the aluminum substrate was applied for the electrospinning process. Then, the resultant fibers were further stabilized in a tube furnace at 200 °C with a heating rate of 5 °C min^{-1} in the air for 30 mins, fellow by annealing at 600 °C for 3 h with a heating rate of 5 °C min^{-1} under Ar atmosphere. The product was washed three times by deionized water to remove the impurity of NaCl. After drying at 60 °C under vacuum overnight, the final desired Sn@CFC sample was obtained. The pure CFC also prepared by the same process but without Sn nanoparticles.

2.2. Structural characterization

The XRD was conducted by a Rigaku SmartLab diffractometer and the Raman spectrum was carried out by LabRAM HR (HORIBA, 532 nm UV laser). TGA was performed with a Perkin Elmer DSC 6000 System instrument up to 800 °C at a heating rate of 10 °C min^{-1} in air. The morphology characterization (SEM, TEM and EDS elemental mapping) were performed using scanning electron microscopy (FESEM, Hitachi, S-4700) and transmission electron microscopy (JEM-2100 LaB6, JEOL).

2.3. Electrochemical measurements

The Sn@CFC and CFC were cut into a 12 mm circular disc as the working electrodes without other treatment. The CR-2035 coin cells were assembled in an argon-filled glove box with sodium foil as the counter electrode, 1.0 M $NaClO_4$ in EC: DMC (1:1 v/v) with 5% FEC as the electrolyte, and a polypropylene film (Celgard-2325) was used as a separator. The electrochemical properties of the Sn@CFC electrode were studied with a multichannel battery-testing system (Neware CT-4008, Shenzhen Neware Co., China). The charge/discharge galvanostatic cycling was evaluated from 2.0 V to 0.01 V. EIS was tested using a VSP (Bio-Logic SAS, France) electrochemical workstation at 25 °C with the frequency ranging from 1 MHz to 0.001 Hz and an AC signal of 10 mV in amplitude as the perturbation. Cyclic voltammogram was carried out using VSP (Bio-Logic SAS, France) electrochemical workstation, the voltage scanned at 0.1–1 mV s^{-1} between 0.01 ~ 2.0 V.

3. Results and discussion

Fig. 1a schematically illustrates the synthesis processes of the Sn@CFC sample. Firstly, the homogenous yellow solution with well-dispersed amorphous SnO was prepared by adding $NaCO_3$ and $SnCl_2$ in DMF according to the Eq. (1), while the by-product NaCl formed precipitation. After adding PAN and with the help of stirring, the mixture of SnO@PAN was electrospun to form a multi-layer fiber cloth. It was then calcined into Sn@CFC in the Ar atmosphere, with carbonizing PAN to carbon and reducing SnO to metallic Sn. The SnO material prepared in deionized water is discussed in the supporting information (Figs. S1–S3).

$$Na_2CO_3(s) + SnCl_2(s) \rightarrow SnO + NaCl(s) + CO_2\uparrow \quad (1)$$

Fig. 1b–d shows the scanning electron microscopy (SEM) images of the as-prepared Sn@CFC sample. As shown in Fig. 1b, the Sn@CFC sample exhibits a 3D cross-linked structure and displays little difference with the SnO@PAN sample (Fig. S4). In addition, the Sn@CFC composites are freestanding and flexible (inset of Fig. 1b), which can be directly used as an electrode material without a binder and a current collector. From Fig. 1c and d, the fiber in Sn@CFC sample has a uniform diameter around 300 nm, and the surface of Sn@CFC sample is rough with Sn nanoparticles successfully embedded in the carbon fiber matrix. The microstructure of the composite is further investigated by transmission electron microscopy (TEM), as shown in Fig. 1e–h. From the Fig. 1e and f, the images further confirm the structure of Sn@CFC sample and agree with the SEM results that the diameter of fibers are almost the same and Sn nanoparticles can be observed both on the surface and inside of the fiber. The particle size of metallic Sn is around 10 nm from the HRTEM image of Fig. 1g. The EDS elemental mapping is shown in Fig. 1h that the Sn and C element are overlapping very well, suggesting that Sn nanoparticles are evenly distributed in the carbon fibers.

The phase of Sn@CFC composite was characterized by X-ray powder diffraction (XRD) measurement. As shown in Fig. 2a, all the intense and instinct peaks can be indexed into tetragonal phase of metallic Sn (β-Sn, JCPDS card no. 04-0673), and a weak broad peak between 20° to 30° is attributed to the amorphous carbon fiber. According to the Scherrer Formula calculation, the average particle size of metallic Sn is larger than that observed from the TEM image. This may be due to the excellent crystallization character of metallic Sn that results in sharp peak, which was widely reported in other nano metallic materials [37,38]. No other peaks of impurities are detected in the XRD pattern, indicating that the final product is made by metallic Sn and amorphous carbon. The amorphous carbon was further confirmed and studied by Raman

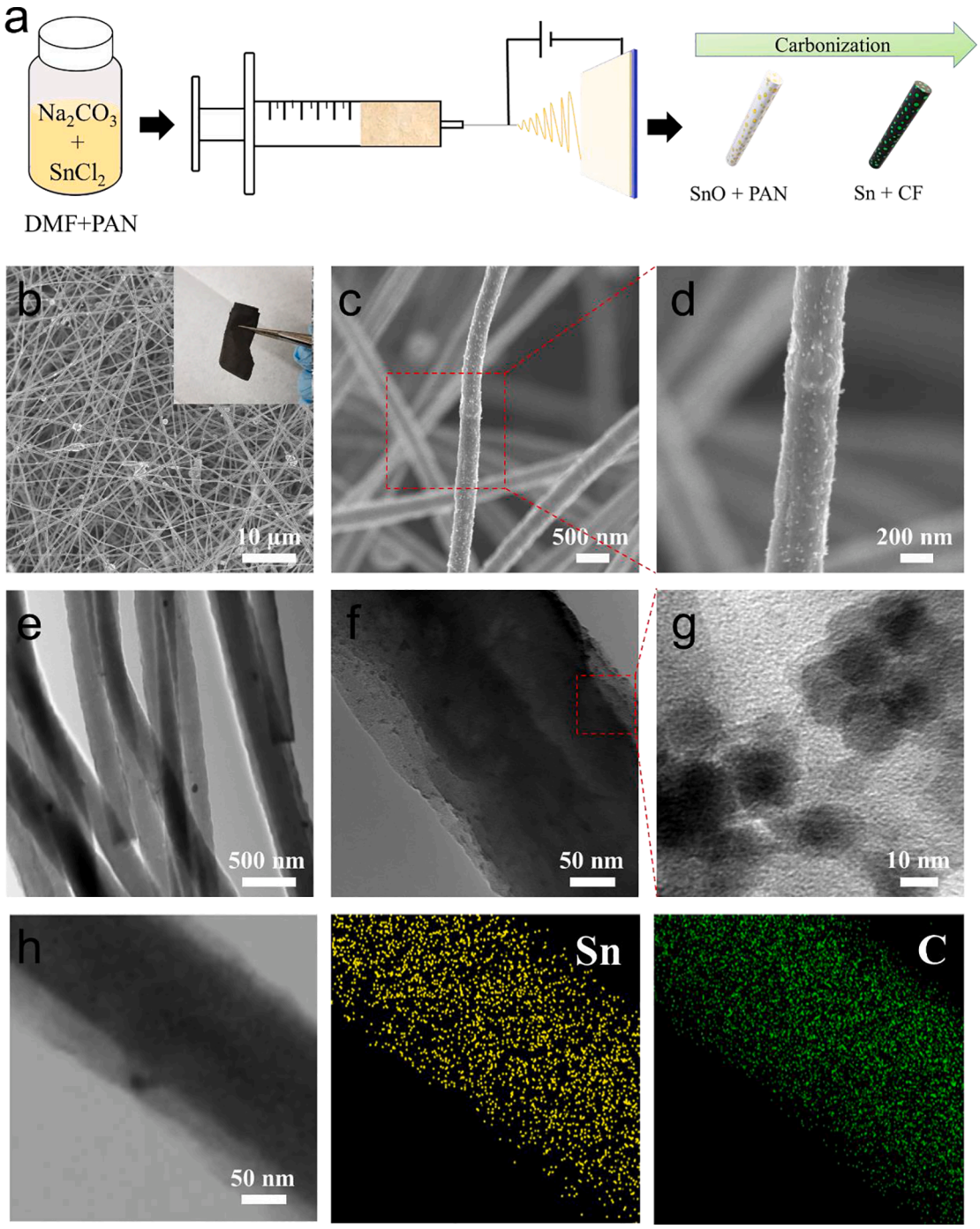

Fig. 1. (a) Schematic illustration of the synthesis of the free-standing Sn@CFC electrode. (b–h) Morphology characterization of Sn@CFC: (a–c) SEM images, (d, e) TEM images, (f) high-resolution TEM image and (g) STEM image with corresponding EDS elemental mappings.

spectra. Fig. 2b shows two peaks located at 1341 cm^{-1} and 1590 cm^{-1} in the Raman spectra, corresponding to D and G bands of amorphous carbon fiber, respectively. I_D/I_G, the intensity ratio of D band and G band that represented the defect quantity for the carbon fiber, was calculated as 1.49 [9,39]. The high ratio of I_D/I_G indicates a large number of defects in the structure, which are capable of improving the electrochemical performance by adsorbing more sodium ions to increase capacitive contribution [40,41]. To detect the weight content of Sn in the composite, thermal gravimetric analysis (TGA) was performed under air from 25 °C to 800 °C. The TGA curve of Sn@CFC in Fig. 2c shows an upward trend and over 100% until 420 °C, which is attributed to the oxidation of metallic tin ($Sn + O_2 \rightarrow SnO_2$). After that, the carbon fibers start to decompose to CO_2 ($C + O_2 \rightarrow CO_2$ (gas)), and the TGA curve displays a general trend of decrease [25,42]. According to the calculation, the content of Sn is 46.7 wt%. The chemical bonding situation of the Sn@CFC sample was analyzed by X-ray photoelectron spectroscopy (XPS). The survey XPS spectrum in Fig. S5 suggests the existence of Sn, C, N and O elements in the sample. The high-resolution C 1s spectrum (Fig. 2d) can be fitted into four peaks at 284.6, 285.2, 286.3 and 287.9 eV originating from C═C, C–C, C═N and C–N, respectively, demonstrating the successful doping of N atoms in the carbon fiber matrix [25]. The N-doping is also confirmed by the high-resolution N 1s spectrum (Fig. 2e), which shows the existence of pyridinic N (398.5 eV), pyrrolic N (399.1 eV) and graphitic N (400.2 eV) [43]. The nitrogen doping is

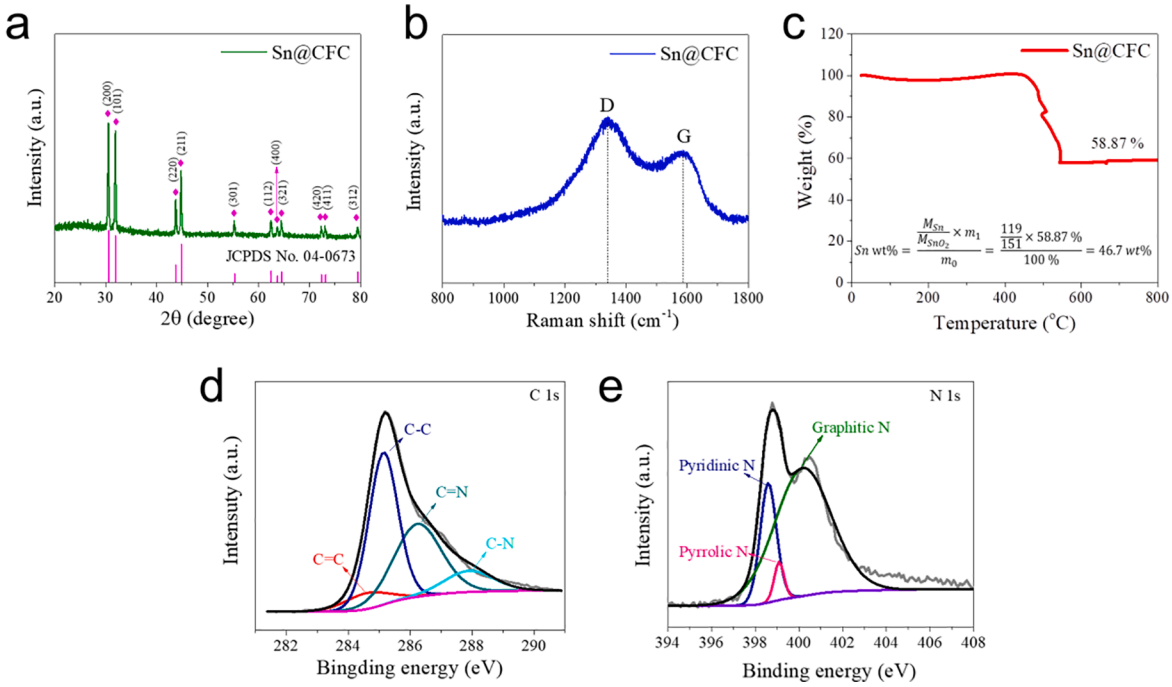

Fig. 2. (a) XRD pattern, (b) Raman spectra and (c) TGA curve of Sn@CFC. XPS spectra of Sn@CFC, (d) C 1s and (e) N 1s.

expected to improve the conductivity of carbon fiber to optimize its charge transfer kinetics, further providing a dominant pseudocapacitance contribution [25,44]. As shown in Fig. S6, there is a pair of characteristic peaks in the high-resolution Sn 3d spectrum at 496.3 and 487.8 eV from Sn $3d_{3/2}$ and Sn $3d_{5/2}$, respectively. The binding energy of $Sn3d_{3/2}$ mainly ascribes to Sn^{4+}, indicating that the surface of the Sn nanoparticles is oxidized due to the exposure in air. The metallic state of Sn was not detected because the XPS data carries only surface information. The similar experimental phenomenon also has been observed in the findings of others [45,46].

The electrochemical properties of the freestanding Sn@CFC electrode for SIBs were systematically studied. The cyclic voltammetry (CV) curves of the initial three cycles at 0.1 mV s^{-1} are shown in Fig. 3a with a voltage range from 0.01 V to 2 V. In the first cathodic scan, there is a board peaks between 1.2 V and 0.6 V, which could be ascribed to the formation of the solid electrolyte interphase (SEI) layer at the electrode/electrolyte interface [29,47]. During the subsequent cathodic process, a sharp redox peak below 0.5 V corresponds to the formation of the $Na_{15}Sn_4$ phase.

$$4\ Sn + 15Na^{+} + 15\ e^{-} \leftrightarrow Na_{15}Sn_4 \quad (2)$$

By comparison, the anodic peak at 0.8 V is observed, suggesting the reversible desodiation reaction of $Na_{15}Sn_4$ phase to the metallic Sn [42,48].

$$Na_{15}Sn_4 \leftrightarrow 4\ Sn + 15Na^{+} + 15\ e^{-} \quad (3)$$

Both cathodic and anodic curves almost overlap in the following CV scans, indicating the high reversibility and good stability of the Sn@CFC electrode. *Ex*-situ XRD patterns of Sn@CFC at different charge-discharge states are used to further specify the electrochemical reactions. Fig. 3b shows the 1st discharge/charge voltage profile of the Sn@CFC electrode at a low current density of 20 mA g^{-1}. There is a small plateau around 1.2 V on the discharge curve, which can be attributed to the formation of SEI film, with the agreement of CV curve above. The voltage of Sn@CFC electrode then rapidly drops to 0.5 V and enters into a long and flat voltage plateau to form the alloy $Na_{15}Sn_4$ phase. In the charge profile, two potential plateaus exhibited at 0.3 V, 0.8 V are the dealloying processes from the $Na_{15}Sn_4$ phase to metallic Sn. *Ex*-situ XRD patterns of Sn@CFC at different charge-discharge states are shown in Fig. 3c. When the Sn@CFC electrode is discharged to 0.5 V, a new phase of $Na_{15}Sn_4$ is observed, indicating the alloy reaction between the metallic Sn and Na^{+} occurs following Eq. (2). After fully discharged to 0.01 V, all peaks belong to the $Na_{15}Sn_4$ phase. When the electrode is charged back, the peaks of Sn reappear at 0.5 V, suggesting the dealloying process from $Na_{15}Sn_4$ to Sn based on Eq. (3). No alloy phase of $Na_{15}Sn_4$ can be detected after the electrode is charged to 1.5 V.

Fig. 3d shows the electrochemical cycling performance of the Sn@CFC at a current density of 50 mA g^{-1}. To demonstrate the excellent structure-property correlation of our Sn@CFC anode. The free-standing CFC electrode was prepared as same as Sn@CFC without metallic Sn for comparison. The first discharge capacity of Sn@CFC electrode is 716 mAh g^{-1} with initial Coulombic Efficiency of 42.25%. However, after that, the CE rise quickly to 92% in the second cycle and top to about 100% in the tenth cycle. The large capacity loss during the first cycle may be due to the formation of an irreversible SEI layer on the surface of the electrode. It should be mentioned that the low initial CE is very common on the free-standing electrode can be addressed by pre-sodiation in the practical application [49,50–52]. The Sn@CFC electrode displays an excellent discharge capacity of 255 mAh g^{-1} after 200 cycles, with an excellent Coulombic efficiency of 99.94%. In particular, the capacity retention is 83.7% from 2nd to 200th cycle, indicating the superior cyclic stability of the Sn@CFC anode. As a comparison, the CFC electrode shows poor cycling performances with a very low capacity. The low capacity of CFC indicates that its contribution to the capacity of Sn@CFC electrode can be negligible. It is noted that the advanced Sn@CFC electrode fully makes use of the huge synergies of nanocrystal Sn particles and the cross-link carbon fiber, giving rise to the excellent electrochemical performances. Specifically, the nano-sized Sn particles can alleviate the strain driving from the large volume change and cross-link carbon fiber can act as a buffer layer to keep the structure stable. In addition, the carbon fiber prevents the direct contact between the metallic Sn particles and the electrolyte, reducing the repeated formation of SEI film during cycles. Fig. 3e shows the 1st, 2nd, 20th and 200th charge/discharge voltage profiles of the Sn@CFC electrode at 50 mA g^{-1}. the discharge/charge voltage plateaus of 2nd, 20th and 200th are nearly overlapped, revealing that the free-standing Sn@CFC anode has a

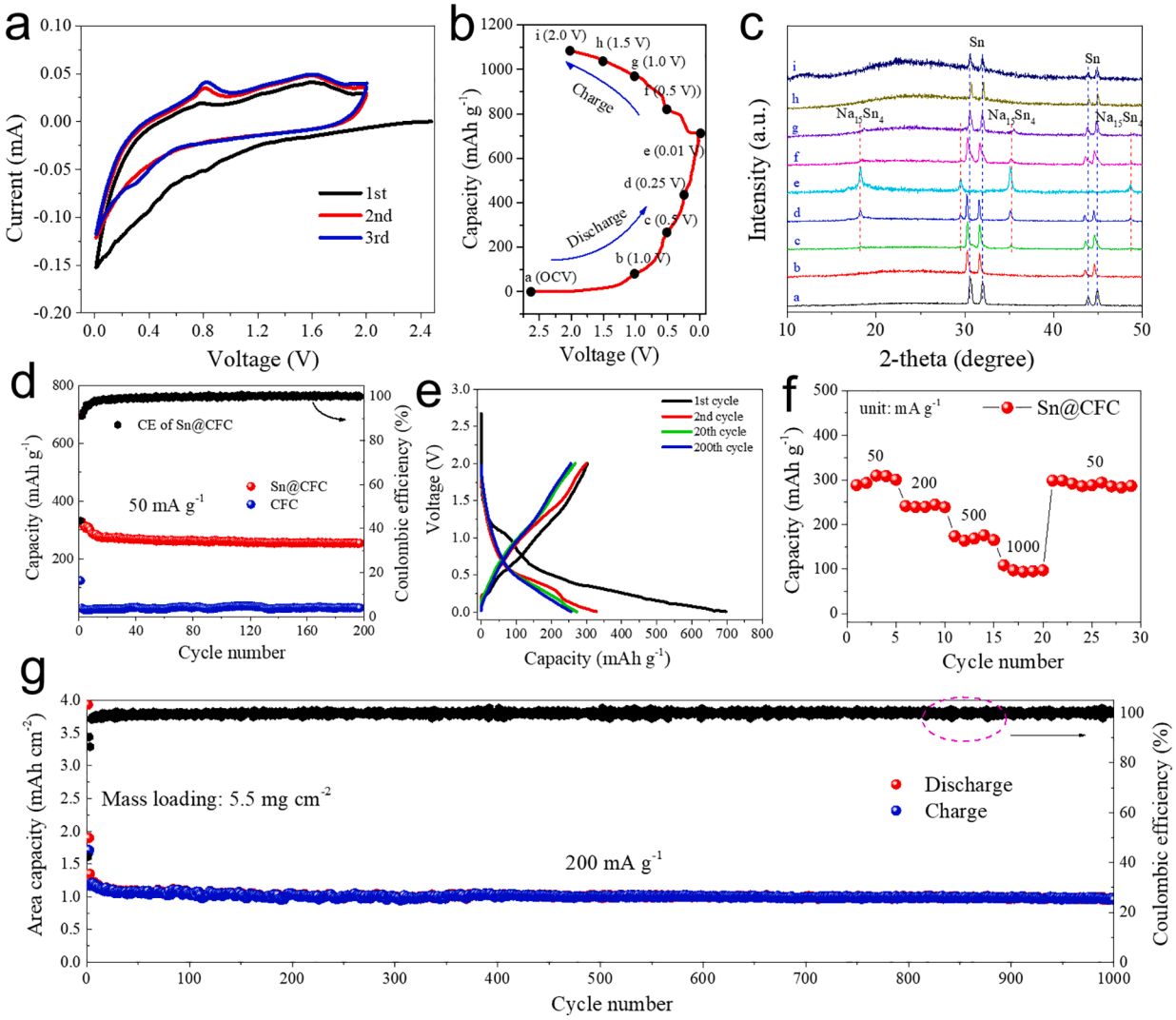

Fig. 3. Electrochemical properties of the Sn@CFC electrode. (a) Cyclic voltammetry curves at a scan rate of 0.1 mV s^{-1} from 0.01 to 2 V. (b) Galvanostatic discharge/charge profiles at the first cycle. (c) *Ex*-situ XRD patterns of Sn@CFC at different charge-discharge states. (d) Cycling performance at 50 mA g^{-1}. (e) Galvanostatic discharge/charge profiles of 1st, 2nd, 20th and 200th cycle at 50 mA g^{-1}. (f) Rate performance at various rates (50 mA g^{-1}–1000 mA g^{-1}). (g) Long-term cycling performance at 200 mA g^{-1}.

stable and reversible electrochemical behavior.

The cross-link carbon fiber also serves as a pathway to transport electrons and ions to increase the conductivity of the Sn@CFC electrode while nano-sized Sn can shorten the diffusion pathway of sodium ions, resulting in good rate capability as shown in Fig. 3f. The rate performance of Sn@CFC was tested at various current densities from 50 mA g^{-1} to 1000 mA g^{-1}. The Sn@CFC electrode provides a high discharge capacity of 310 mAh g^{-1} at 50 mA g^{-1}, 246 mAh g^{-1} at 200 mA g^{-1}, 170 mAh g^{-1} at 500 mA g^{-1}. Even at a very high current density of 1000 mA g^{-1}, the Sn@CFC anode can still deliver a capacity of more than 100 mAh g^{-1}, holding the high potential for the fast-charging applications. Furthermore, a capacity of more than 300 mAh g^{-1} can be retained when the current density drops back to 50 mA g^{-1} after various current densities, indicating that the Sn@CFC anode has an excellent rate performance and cycling stability. As mentioned in the introduction part, the SIBs are suitable for large-scale stationary energy storage applications. Hence, it is essential to develop electrodes with both high mass loading and excellent electrochemical performance, especially for a long lifetime to meet the requirement of maintenance-free or maintenance-little energy storage devices. The as-prepared Sn@CFC electrodes without current collector based on our scalable manufacturing technique can achieve both high mass loading and long cycle life. The long-life performance of the Sn@CFC electrode with high mass loading of 5.5 mg cm^{-2} is investigated at a high current density of 200 mA g^{-1} for 1000 cycles after the activation at a small current density of 50 mA g^{-1} for the initial two cycles. As shown in Fig. 3g, after cycling up to 1000 cycles, the Sn@CFC electrode can deliver a high areal capacity of 1 mAh cm^{-2} and the capacity retention of the Sn@CFC electrode is more than 80% from 3rd to 1000th cycle, with an average loss over 1000 total cycles of only 0.02% per cycle, indicating excellent cycling stability. We also compare the electrochemical performances of our Sn@CFC composite with some other Sn-based anode materials for SIBs, exhibited in Table S1. It can be concluded from the table that the research on the high mass loading, which plays an important role in energy density and fabrication cost, is still limited and the areal capacity is inferior. Our novel Sn@CFC electrode shows superior cycling stability over 1000 cycles with high mass loading of 5.5 mg cm^{-2}.

Fig. 4a shows the structure revolution schematic of the free-standing Sn@CFC electrode. The free-standing Sn@CFC electrode with high mass loading can keep the structure stable after long cycle life, profiting from the cross-link 3D structure and ultrasmall Sn particles. First, the carbon fiber can act as the channels for both electrons' and ions' to greatly improve the conductivity of the electrode and diffusion speed of sodium ions. Hence, it can significantly reduce the polarization effects to make

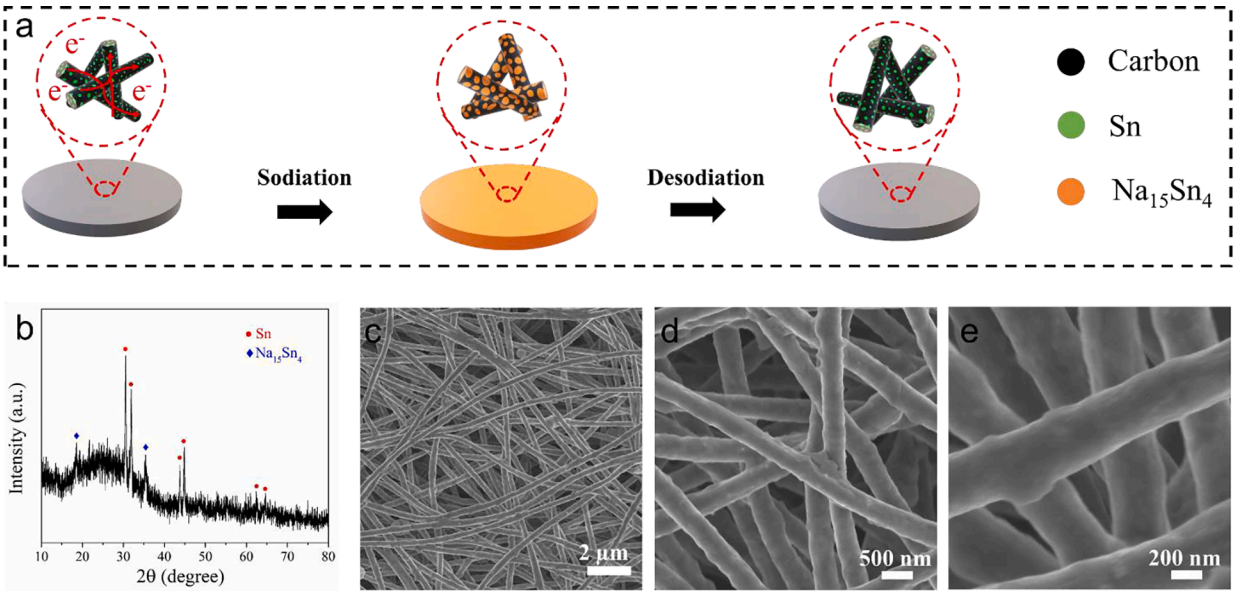

Fig. 4. (a) Schematic illustration of the structure revolution of the free-standing Sn@CFC electrode. (b) XRD of Sn@CFC after 200 cycles (charge to 1.0 V), (c–e) SEM images of the Sn-CFC electrode after 200 cycles.

sure more active materials involving electrochemical process in a thick electrode. Second, the carbon fiber skeleton has a cross-link 3D structure that can form strong adhesion between the fibers to prevent the electrode delamination, and the free-standing design can make electrolyte penetration through a thick electrode easily. Third, the ultrasmall particle can mitigate the strain generated from the alloying and dealloying processes and the carbon matrix can buffer the volume expansion, which in turn enable that the Sn particles embedded in carbon fiber do not crush and aggerate to ensure excellent cyclic performance. Hence, the Sn@CFC electrode prepared by the scalable electrospinning technique offers a promising route to synthesize high-mass-loading electrode for SIBs to satisfy the demand in large-scale stationary energy storage application. For better understanding the structure stability of Sn@CFC sample after long-life cycling, the electrode was taken out from the battery after 200 cycles at 200 mA g^{-1} with the battery charged to 1.0 V and washed by the DMC solution to clear the electrolyte coating on the surface on the electrode. The photographs of the free-standing Sn@CFC electrode after 200 cycles are provided in Fig. S7. The electrode has an integrated structure without any crush compared to the electrode before the cycle, and it shows great flexibility. The XRD pattern of the Sn@CFC electrode over 200 long-life cycles has been provided in Fig. 4b. The phase of metallic Sn and alloy $Na_{15}Sn_4$ can still be observed in the XRD pattern after 200 cycles, indicating that the metallic Sn phase inside the carbon fiber is reversible during repeated sodiation/desodiation processes. Moreover, the SEM images from Fig. 4c–e reveal that the structure of the Sn@CFC keeps almost the same compared with the images before cycle (Fig. 1b–d), demonstrating outstanding structure stability. Meanwhile, despite the expansion of the Sn after alloyed with sodium, there are no obvious crashing Sn particles in the electrode, indicating that the carbon as the buffer layer can significantly alleviate the strain driving from the volume change and prevent the pulverization of the metallic Sn phase. Moreover, a thin and smooth SEI layer, which can protect the Sn particles to contact with the electrolyte, is found on the surface of the composite. It can be attribute to the existence of the carbon layer, and widely reported in other papers [3,53]. To demonstrate the excellent structure-property correlation of our Sn@CFC anode, the commonly reported Sn@C are fabricated and characterized. The details and discussion are provided in supporting information (Figs. S8–S13).

Electrochemical kinetic properties of the Sn@CFC electrode were further studied by testing CV at various scan rates from 0.1 mV s^{-1} to 1 mV s^{-1} to clarify the contributions from capacitive and diffusion-controlled behaviors. Capacitive-controlled behavior is also known as pseudocapacitance, which is defined as a faradaic charge transfer on the surface or near-surface region, exhibiting capacitor-like properties to achieve ultrafast charge storage [54,55]. Pseudocapacitance can emerge when a battery material is engineered at the nanoscale with a large fraction of Na^+ storage sites [56,57]. Fig. 5a shows the CV curves at different scan rates. The CV curves display a similar sharp while the peaks grow gradually with the increase of the scan rate. The relationship between the peak current (i) and the sweep rate (v) could be described by the power law as shown in Eq. (4), where a and b are adjustable values [58–60].

$$i = av^b \tag{4}$$

When the b value is 0.5, it indicates the diffusion-controlled behavior, while the surface-controlled capacitive reaction dominates for the value of 1. As shown in Fig. 5b, the b values of cathodic peak and anodic peak are 0.68 and 0.78, respectively, according to the calculation by the slope of log (i) versus log (v) plots. The b values of both peak cathodic peak and anodic peak are between 0.5 and 1, indicating both diffusion-controlled behavior and capacitive reaction play important roles in contributing capacity. The ratio of capacitive contribution is expressed by the Eq. (5), in which k_1v is the capacitive contribution and $k_2v^{1/2}$ is the contribution from diffusion-controlled processes (k_1 and k_2 are variable constants) [58,59,61].

$$i = k_1v + k_2v^{1/2} \tag{5}$$

$$i(V)/v^{1/2} = k_1v^{1/2} + k_2 \tag{6}$$

If both sides of Eq. (5) are divided by $v^{1/2}$ then it becomes Eq. (6). By plotting the $v^{1/2}$ vs $i/v^{1/2}$ at different scan rates at a fixed voltage, the specific value of k_1 and k_2 was determined from the slope. For example, Fig. 5c shows the CV curve and the capacitive contribution (shade area) at 0.5 mV s^{-1}, suggesting that the ratio of capacitive contribution is 87.1%. In the Fig. 5d, the ratio capacitive contribution displays a rising trend with the increase of scan rate, from 60.7% at 0.1 mV s^{-1} up to 87.1% at 0.5 mV s^{-1}, indicating that the capacitive contribution plays an important role at high rate of the Sn@CFC electrode. Therefore, the Sn@CFC electrode shows a good rate performance and delivers a high area capacity at a high current density.

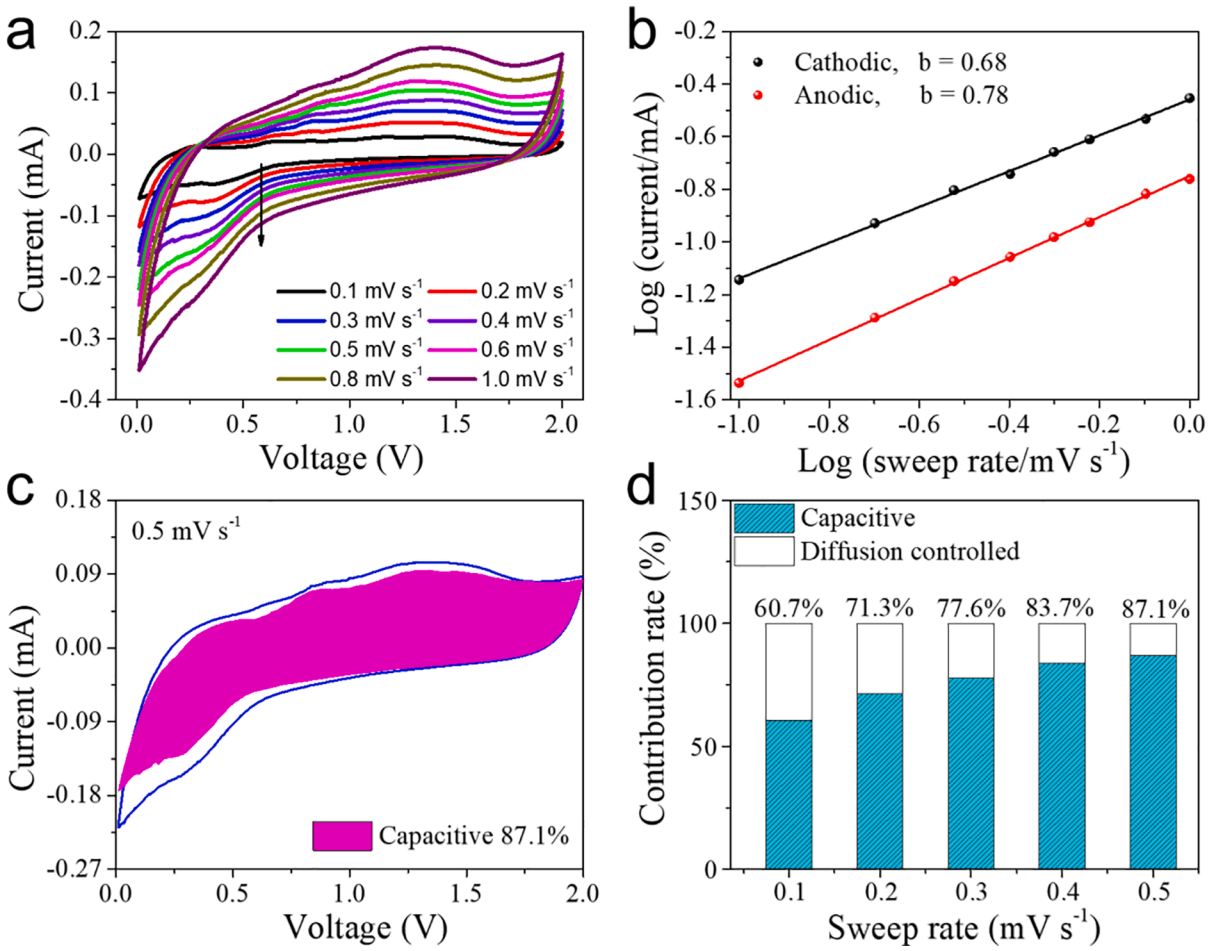

Fig. 5. The electrochemical kinetic properties of the Sn@CFC anode. (a) CV curves at various scan rate from 0.1 mV s^{-1} to 1 mV s^{-1}. (b) The corresponding curves log i vs. log v for the cathodic and anodic peak. (c) CV curve and the capacitive contribution (shaded area) at 0.5 mV s^{-1}. (d) The capacitive contribution in percentage at different scan rates.

4. Conclusion

In summary, we performed a facile and scalable electrospinning method for a high-mass-loading free-standing Sn-based anode that nanosized metallic Sn particles are uniformly embedded in the carbon fiber. The Sn@CFC electrodes deliver an ultra-long cycle life with high areal capacity and an improved rate capability due to the successful synergic effect of ultrasmall Sn nanoparticles and the N-doping 3D carbon fibers, which (1) the ultrafine Sn metallic particles significantly shorten the pathway of sodium ions and electrons; (2) the 3D crosslink carbon fiber act as buffer layer to mitigate the volume expansion and enhance the electronic conductivity. In addition, the kinetic analyses indicate that the capacitive reactions play an important role in contributing capacity, leading to a good rate performance and delivers a high area capacity at a high current density. This work not only provides a highly simple and scalable method to fabricate an anode material with high areal capacity and high energy density but also sheds lights for effective design and development of advanced anodes for SIBs in further practical applications.

Declaration of Competing Interest

The authors declare that they have no known competing financial interests or personal relationships that could have appeared to influence the work reported in this paper.

Acknowledgements

The authors acknowledge from NASA EPSCoR (NNX14AN22A), NSF-MRI (1428992), SD BoR competitive Research Grant program (CRGP), SD BoR Research & Development Grant, NSF IUCRC Planning Program (1841502).

Appendix A. Supplementary data

Supplementary data to this article can be found online at https://doi.org/10.1016/j.cej.2021.128638.

References

[1] B. Scrosati, J. Hassoun, Y.-K. Sun, Energy Environ. Sci. 4 (2011) 3287–3295.
[2] Y. Liu, Y. Zhu, Y. Cui, Nat. Energy 4 (2019) 540–550.
[3] P. Xue, N. Wang, Z. Fang, Z. Lu, X. Xu, L. Wang, Y. Du, X. Ren, Z. Bai, S. Dou, G. Yu, Nano Lett. 19 (2019) 1998–2004.
[4] Z. Li, Y. Dong, J. Feng, T. Xu, H. Ren, C. Gao, Y. Li, M. Cheng, W. Wu, M. Wu, ACS Nano (2019).
[5] S. Wang, X.B. Zhang, Adv. Mater. 31 (2019), e1805432.
[6] Y. Fang, X.-Y. Yu, X.W. Lou, Adv. Mater. 30 (2018) 1706668.
[7] C. Vaalma, D. Buchholz, M. Weil, S. Passerini, Nat. Rev. Mater. 3 (2018) 18013.
[8] P.K. Allan, J.M. Griffin, A. Darwiche, O.J. Borkiewicz, K.M. Wiaderek, K. W. Chapman, A.J. Morris, P.J. Chupas, L. Monconduit, C.P. Grey, J. Am. Chem. Soc. 138 (2016) 2352–2365.
[9] J. Chen, X. Fan, X. Ji, T. Gao, S. Hou, X. Zhou, L. Wang, F. Wang, C. Yang, L. Chen, C. Wang, Energy Environ. Sci. 11 (2018) 1218–1225.
[10] N. Sun, Z. Guan, Y. Liu, Y. Cao, Q. Zhu, H. Liu, Z. Wang, P. Zhang, B. Xu, Adv. Energy Mater. 9 (2019) 1901351.

[11] K. Li, J. Zhang, D. Lin, D.W. Wang, B. Li, W. Lv, S. Sun, Y.B. He, F. Kang, Q.H. Yang, L. Zhou, T.Y. Zhang, Nat. Commun. 10 (2019) 725.
[12] D. Zhao, R. Zhao, S. Dong, X. Miao, Z. Zhang, C. Wang, L. Yin, Energy Environ. Sci. 12 (2019) 2422–2432.
[13] S. Wang, Y. Fang, X. Wang, X.W. Lou, Angew. Chem. Int. Ed. 58 (2019) 760–763.
[14] Y. Liu, B. Zhou, S. Liu, Q. Ma, W.-H. Zhang, ACS Nano 13 (2019) 5885–5892.
[15] C. Cui, J. Xu, Y. Zhang, Z. Wei, M. Mao, X. Lian, S. Wang, C. Yang, X. Fan, J. Ma, C. Wang, Nano Lett. 19 (2019) 538–544.
[16] B. Zhang, G. Rousse, D. Foix, R. Dugas, D.A. Corte, J.M. Tarascon, Adv. Mater. 28 (2016) 9824–9830.
[17] X. Yang, R.-Y. Zhang, J. Zhao, Z.-X. Wei, D.-X. Wang, X.-F. Bie, Y. Gao, J. Wang, F. Du, G. Chen, Adv. Energy Mater. 8 (2018) 1701827.
[18] Y. Liu, N. Zhang, L. Jiao, J. Chen, Adv. Mater. 27 (2015) 6702–6707.
[19] T. Palaniselvam, M. Goktas, B. Anothumakkool, Y.N. Sun, R. Schmuch, L. Zhao, B. H. Han, M. Winter, P. Adelhelm, Adv. Funct. Mater. 29 (2019) 1900790.
[20] Y. Wang, Y. Zhang, J. Shi, X. Kong, X. Cao, S. Liang, G. Cao, A. Pan, Energy Storage Mater. 18 (2019) 366–374.
[21] H. Zhang, X. Huang, O. Noonan, L. Zhou, C. Yu, Adv. Funct. Mater. 27 (2017) 1606023.
[22] S. Li, Z. Wang, J. Liu, L. Yang, Y. Guo, L. Cheng, M. Lei, W. Wang, ACS Appl. Mater. Interfaces 8 (2016) 19438–19445.
[23] Y. Zhao, A. Manthiram, Chem. Mater. 27 (2015) 3096–3101.
[24] P.R. Abel, M.G. Fields, A. Heller, C.B. Mullins, ACS Appl. Mater. Interfaces 6 (2014) 15860–15867.
[25] L. Pan, H. Huang, M. Zhong, M. Niederberger, Energy Storage Mater. 16 (2019) 519–526.
[26] W. Song, X. Liu, B. Wu, N. Brandon, P.R. Shearing, D.J.L. Brett, F. Xie, D. Jason Riley, Energy Storage Mater. 18 (2019) 229–237.
[27] X. Xie, K. Kretschmer, J. Zhang, B. Sun, D. Su, G. Wang, Nano Energy 13 (2015) 208–217.
[28] Y. Liu, N. Zhang, L. Jiao, Z. Tao, J. Chen, Adv. Funct. Mater. 25 (2015) 214–220.
[29] S. Chen, Z. Ao, B. Sun, X. Xie, G. Wang, Energy Storage Mater. 5 (2016) 180–190.
[30] X. Ren, J. Wang, D. Zhu, Q. Li, W. Tian, L. Wang, J. Zhang, L. Miao, P.K. Chu, K. Huo, Nano Energy 54 (2018) 322–330.
[31] W. Ma, K. Yin, H. Gao, J. Niu, Z. Peng, Z. Zhang, Nano Energy 54 (2018) 349–359.
[32] D. Lin, Z. Lu, P.-C. Hsu, H.R. Lee, N. Liu, J. Zhao, H. Wang, C. Liu, Y. Cui, Energy Environ. Sci. 8 (2015) 2371–2376.
[33] L. Hu, F. La Mantia, H. Wu, X. Xie, J. McDonough, M. Pasta, Y. Cui, Adv. Energy Mater. 1 (2011) 1012–1017.
[34] R. Yi, J. Zai, F. Dai, M.L. Gordin, D. Wang, Nano Energy 6 (2014) 211–218.
[35] Q. Gan, H. He, Y. Zhu, Z. Wang, N. Qin, S. Gu, Z. Li, W. Luo, Z. Lu, ACS Nano 13 (2019) 9247–9258.
[36] P. Xiong, P. Bai, A. Li, B. Li, M. Cheng, Y. Chen, S. Huang, Q. Jiang, X.-H. Bu, Y. Xu, Adv. Mater. 31 (2019) 1904771.
[37] R. Mo, X. Tan, F. Li, R. Tao, J. Xu, D. Kong, Z. Wang, B. Xu, X. Wang, C. Wang, J. Li, Y. Peng, Y. Lu, Nat. Commun. 11 (2020) 1374.
[38] Y. Xu, Q. Liu, Y. Zhu, Y. Liu, A. Langrock, M.R. Zachariah, C. Wang, Nano Lett. 13 (2013) 470–474.
[39] Z. Wu, G. Liang, W.K. Pang, T. Zhou, Z. Cheng, W. Zhang, Y. Liu, B. Johannessen, Z. Guo, Adv. Mater. 32 (2020) 1905632.
[40] Z. Wu, B. Li, Y. Xue, J. Li, Y. Zhang, F. Gao, J. Mater. Chem. A 3 (2015) 19445–19454.
[41] J. Niu, R. Shao, J. Liang, M. Dou, Z. Li, Y. Huang, F. Wang, Nano Energy 36 (2017) 322–330.
[42] H. Ying, S. Zhang, Z. Meng, Z. Sun, W.-Q. Han, J. Mater. Chem. A 5 (2017) 8334–8342.
[43] H. Qiu, L. Zhao, M. Asif, X. Huang, T. Tang, W. Li, T. Zhang, T. Shen, Y. Hou, Energy Environ. Sci. 13 (2020) 571–578.
[44] S. Mu, Q. Liu, P. Kidkhunthod, X. Zhou, W. Wang, Y. Tang, Natl. Sci. Rev. (2020).
[45] F. Zhang, Y. Wang, W. Guo, S. Rao, P. Mao, Chem. Eng. J. 360 (2019) 1509–1516.
[46] X. Chang, T. Wang, Z. Liu, X. Zheng, J. Zheng, X. Li, Nano Res. 10 (2017) 1950–1958.
[47] Y. Xu, Y. Zhu, Y. Liu, C. Wang, Adv. Energy Mater. 3 (2013) 128–133.
[48] M. Mao, F. Yan, C. Cui, J. Ma, M. Zhang, T. Wang, C. Wang, Nano Lett. 17 (2017) 3830–3836.
[49] S. Wang, L. Xia, L. Yu, L. Zhang, H. Wang, X.W. Lou, Adv. Energy Mater. 6 (2016) 1502217.
[50] L. Wang, G. Yang, J. Wang, S. Wang, C. Wang, S. Peng, W. Yan, S. Ramakrishna, Small 15 (2019) 1901584.
[51] W. He, Y. Liang, H. Tian, S. Zhang, Z. Meng, W.-Q. Han, Energy Storage Mater. 8 (2017) 119–126.
[52] X.-L. Wang, W.-Q. Han, H. Chen, J. Bai, T.A. Tyson, X.-Q. Yu, X.-J. Wang, X.-Q. Yang, J. Am. Chem. Soc. 133 (2011) 20692–20695.
[53] L. Ji, M. Gu, Y. Shao, X. Li, M.H. Engelhard, B.W. Arey, W. Wang, Z. Nie, J. Xiao, C. Wang, J.-G. Zhang, J. Liu, Adv. Mater. 26 (2014) 2901–2908.
[54] P. Simon, Y. Gogotsi, B. Dunn, Science 343 (2014) 1210–1211.
[55] K. Yao, Z. Xu, M. Ma, J. Li, F. Lu, J. Huang, Adv. Funct. Mater. 30 (2020) 2001484.
[56] Y. Wang, Y. Song, Y. Xia, Chem. Soc. Rev. 45 (2016) 5925–5950.
[57] S. Lou, X. Cheng, Y. Zhao, A. Lushington, J. Gao, Q. Li, P. Zuo, B. Wang, Y. Gao, Y. Ma, C. Du, G. Yin, X. Sun, Nano Energy 34 (2017) 15–25.
[58] P. Li, J.Y. Hwang, Y.K. Sun, ACS Nano 13 (2019) 2624–2633.
[59] B.H. Hou, Y.Y. Wang, Q.L. Ning, W.H. Li, X.T. Xi, X. Yang, H.J. Liang, X. Feng, X. L. Wu, Adv. Mater. (2019), e1903125.
[60] K. Yao, Z. Xu, J. Huang, M. Ma, L. Fu, X. Shen, J. Li, M. Fu, Small 15 (2019) 1805405.
[61] L. Shen, Y. Wang, H. Lv, S. Chen, P.A. van Aken, X. Wu, J. Maier, Y. Yu, Adv. Mater. 30 (2018), e1804378.